Chemical Engineering Journal 497 (2024) 154487

Contents lists available at ScienceDirect

Chemical Engineering Journal

journal homepage: www.elsevier.com/locate/cej

High-Efficiency NO conversion via In-Situ grown covalent organic framework on g-C_3N_4 nanosheets with Single-Atom platinum photocatalyst

Zhiyu Xiao [a], Abubakar Yusuf [a], Yong Ren [b,*], George Zheng Chen [c], Chengjun Wang [d], Jun He [a,e,*]

[a] Department of Chemical and Environmental Engineering, University of Nottingham Ningbo China, Ningbo, Zhejiang, 315100, China
[b] Department of Mechanical, Materials and Manufacturing Engineering, University of Nottingham Ningbo China, Ningbo, Zhejiang, 315100, China
[c] Department of Chemical and Environmental Engineering, University of Nottingham, Nottingham NG7 2RD, UK
[d] College of Resources and Environmental Sciences, South-Central Minzu University, Wuhan, Hubei, 430074, China
[e] Nottingham Ningbo China Beacons of Excellence Research and Innovations Institute, Ningbo, Zhejiang, 315032, China

ARTICLE INFO

Keywords:
Chemically Bonded Heterostructure
Covalent Organic Framework
In-situ Growth
Photocatalytic NO Removal
Platinum Redox Cycle

ABSTRACT

This study presents a chemically bonded Pt/TP-BPY-CN/g-C_3N_4 composite photocatalyst created through an in-situ growth method via Schiff base reaction between g-C_3N_4 and aldehyde-functionalized TP-BPY-COF. The −H-C-N-H- bonds formed at the g-C_3N_4 and TP-BPY-COF interface significantly boost electron communication, thereby substantially enhancing transfer efficiency between these two constituents. Besides, single-atom platinum incorporation via coordination establishes a Pt^{2+}/Pt^{4+} redox cycle, aiding both oxidation and reduction of nitric oxide (NO). Consequently, the Pt/40TPBPY-CN composite achieves 65.3 % NO conversion, with almost 100 % oxidation selectivity towards NO_3^-. In-situ XPS analysis confirms the robust electron communication between TP-BPY-COF and g-C_3N_4 facilitated by −H-C-N-H- bonds, and the redox transformation between Pt^{2+} and Pt^{4+}. In addition, DFT calculation provides a deeper insight into photocatalytic oxidation and reduction pathways, confirming an inhibition of N_2 desorption. This research underscores the benefits of chemically bonded heterostructures for improved electronic interactions and highlights the efficacy of bifunctional single-atom platinum in photocatalysis.

1. Introduction

The rapid urbanization and industrialization of the modern world have brought with them numerous challenges, one of the most pressing being the issue of air pollution [1]. Nitrogen oxides (NO_x), primarily nitrogen monoxide (NO) and nitrogen dioxide (NO_2), are among the major contributors to air pollution, with deleterious effects on human health and the environment [2,3]. NO as a colorless and toxic gas, when exposed to sunlight, contributes to the formation of ground-level ozone and particulate matter, further exacerbating air quality issues [4,5]. The need for effective and sustainable methods to combat NO pollution has become an urgent priority in environmental science.

Photocatalytic degradation has emerged as a promising avenue for NO_x removal from the atmosphere [6,7]. The ability of semiconductors to initiate chemical reactions upon exposure to light has spurred interest in harnessing this principle for environmental remediation [7]. Visible light-driven photocatalysts have garnered attention due to their energy efficiency and practicality in harnessing natural light resources [8]. However, the relative inefficiency of photocatalysis remains a significant hurdle in the quest for effective NO removal, thus demanding a concerted research effort to elevate photocatalytic performance.

Previous studies have highlighted that the construction of a Z-scheme heterojunction between g-C_3N_4 and other semiconductors can significantly boost the photocatalytic oxidation efficiency of NO [9,10]. This enhancement is primarily attributed to the improved separation of photogenerated electrons and holes, along with accelerated electron transfer. To further augment the synergistic effects within these heterojunction composites, it is crucial to optimize various interface factors such as band structure compatibility, interfacial driving force, and contact area [11,12]. These optimizations aim to enhance the carrier separation and transfer processes across the materials. For instance, Wu and Kang et al. [11] have demonstrated a 2D/2D layered $BiOIO_3$/g-C_3N_4 Z-scheme heterojunction that achieved a 46.9 % photocatalytic efficiency, which was significantly attributed to the improved efficiency of

* Corresponding authors.
E-mail addresses: yong.ren@nottingham.edu.cn (Y. Ren), jun.he@nottingham.edu.cn (J. He).

https://doi.org/10.1016/j.cej.2024.154487
Received 24 June 2024; Received in revised form 27 July 2024; Accepted 31 July 2024
Available online 3 August 2024
1385-8947/© 2024 The Author(s). Published by Elsevier B.V. This is an open access article under the CC BY-NC license (http://creativecommons.org/licenses/by-nc/4.0/).

interfacial carrier separation. However, the interface between these integrated materials often exhibits relative weakness, predominantly due to direct contact governed by Van der Waals forces. Addtionally, a fixed nanosheet structure of g-C_3N_4 that does not provide sufficient pores for NO and light adsorption. It is essential to investigate the enhancement of interfacial driving forces and optimization of interface between these composites to further improve electron communication between integrated materials.

In recent years, covalent organic frameworks (COFs) have obtained substantial interest in the field of environment treatment due to their unique properties, such as tunable bandgaps, high surface areas, and exceptional chemical stability [13]. COFs are an emerging class of crystalline, porous, and covalent organic materials that can be precisely designed and synthesized [14]. These materials offer a versatile platform for tailoring the electronic structure and surface chemistry, making them excellent candidates for water treatment technology, energy storage, adsorption and separation [15–19]. For example, Ifthikar et al. demonstrated the efficient reduction of V(V) to V(IV) and adsorption of V species by controlled organic group such as − SH, =NH and − NH−, carried out a reliable techology for wastewater treatment system [20]. In terms of energy storage, Lv and Tan et al. reported a covalent organic framework integrating naphthalene diimide and triphenylamine units, achieving a solar Li-ion battery with a 38.7 % increase in efficiency when NT-COF is applied as the cathode material [21]. Building on these versatile applications, COFs exhibit significant potential in photocatalysis, providing promising solutions for environmental remediation such as the photocatalytic oxidation of NO [22]. Notably, COF-based composites synthesized through in-situ growth techniques have demonstrated remarkable advancements, enabling precise control over the material's morphology and significantly enhancing their photocatalytic performance. For instance, Zhang and Hu et al. developed a novel COF/metal oxide (COF/MOx) Z-scheme heterojunction via in-situ self-polymerization. This study involved coating a hydrophobic COF on the surface of TiO_2, offering an innovative optimization method for the heterostructure interface, which facilitated increased separation of photogenerated carriers and improved light capture capability [23]. This research not only underscored the profound impact of heterostructure interfaces on photocatalytic performance but also introduced a new pathway for the optimization of COF-based photocatalysts, paving the way for the in-situ growth of COF materials on nanosheet g-C_3N_4. The inherent properties of COFs could enable the formation of chemically-linked heterostructures with g-C_3N_4, further enhancing interfacial driving forces and providing tunable characteristics for composite materials. Additionally, the in-situ growth of COF materials on nanosheet g-C_3N_4 can significantly offset the low porosity, and limited light and NO adsorption of g-C_3N_4, thanks to the porous structure of COF materials. Among various COF materials, bipyridine-based COFs have attracted considerable attention due to their capability to immobilize metal single atoms or nanoparticles, showcasing high potential in both photocatalysis and electrochemical catalysis. [15,24–26]. For example, Li and Yang et al. [26] have demonstrated that a Pt-COF_{800} catalyst exhibits exceptional activity for the oxygen reduction reaction. They confirmed the coexistence of platinum single atoms and nanoparticles, highlighting the substantial impact of nanoparticle platinum on catalyst performance. Additionally, Yang and Chu et al. [15] studied Pt@TpBpy-NS photocatalysts for water splitting applications, achieving a 0.23 % solar-to-hydrogen efficiency by incorporating platinum nanoparticles into the pores of COF nanosheets. This research underscores the significance of platinum nanoparticles in the applications of bipyridine-based COFs. However, research on the effects of single-atom platinum coordinated on COFs in photocatalysis is limited. The presence of single atoms not only contributes to a high atom utilization rate but also facilitates a higher density of active sites during photocatalytic reactions [27]. The synergy between bipyridine-based COFs and g-C_3N_4, coupled with the coordination of single-atom platinum, presents an exciting opportunity to enhance the relatively low photocatalytic performance in NO degradation.

Our research delves into the in-situ formation of TP-BPY-COF on the nanosheet architecture of g-C_3N_4. This formation is driven by a Schiff base reaction, which enables the integration of TP-BPY-COF onto the g-C_3N_4 surface through the interaction between aldehyde groups in TP-BPY-COF and amine groups on g-C_3N_4, resulting in covalent bonding and subsequent COF growth. Notably, electron transfer within this system is facilitated by novel −H-C=N-H chemical bonds, which provide a stronger interfacial driving force compared to direct loading composites. Moreover, we incorporate single atom platinum into the TP-BPY-CN (TP-BPY-COF/g-C_3N_4) photocatalysts via a chelation reaction to further investigate the enhancement mechanisms provided by single atoms. In this context, single atom platinum, incorporated into the porous structure of TP-BPY-CN, serves as the principal active site, significantly boosting photocatalytic efficiency. This innovative approach not only establishes a covalently bonded binary heterostructure, ensuring superior electron transfer capabilities compared to conventional methods of material integration onto g-C_3N_4 surfaces, optimizes the overall porous structure of g-C_3N_4, providing more active sites for NO and light adsorption. Additionally, the precise coordination of single atoms on the bipyridine units within TP-BPY-COF introduces a distinctive mechanism that markedly enhances photocatalytic efficiency, highlighting the critical role of single atoms in optimizing photocatalytic processes.

2. Materials and methods

2.1. Catalyst preparation

Nanosheet g-C_3N_4(CN): Nanosheet CN was prepared following a well-established procedure [28]. Initially, Initially, 4 g of melamine were placed into a 30 mL alumina crucible, covered, and then subjected to a heat treatment in a muffle furnace at 550 °C for 4 h to yield the final product. Subsequently, the resulting product was pulverized and prepared for subsequent use.

TP-BPY-COF: The preparation of TP-BPY-COF was conducted following previously reported methods with slight adaptations [26]. Specifically, 27.9 mg of 2,2′-bipyridine-5,5′-diamine (0.15 mmol) and 21 mg of 1,3,5-Triformylphloroglucinol (Tp) (0.1 mmol) were loaded into a 10 mL Pyrex tube. A solvent mixture comprising 1.5 mL of N,N-Dimethylacetamide (DMAc) and 0.5 mL of o-Dichlorobenzene (o-DCB) was employed. Following 30 min of ultrasonication at room temperature, the mixture was cryogenically frozen in a liquid nitrogen bath (77 K) and subsequently evacuated after three freeze–pump–thaw cycles. The homogeneous solution was then transferred to an oven and subjected to a 72-hour heating process at 120 °C. The resulting precipitate was separated via filtration and underwent triple washing with tetrahydrofuran. Finally, the product was purified using Soxhlet extraction in tetrahydrofuran for 24 h and subsequently dried under vacuum at 60 °C to yield TP-BPY-COF.

TPBPY-CN: The synthesis of TPBPY-CN is identical to that of TP-BPY-COF, with the addition of a specific amount of g-C_3N_4. Various mass fractions of TP-BPY-COF were synthesized and denoted as XTPBPY-CN (where X represents the mass fraction of TP-BPY-COF).

Pt/TPBPY-CN: To prepare Pt-TPBPY-CN, 200 mg of the synthesized TPBPY-CN was mixed with a calculated amount of 18 % platinum nitrate solution. An 80 mL mixture of ethanol and methanol in a 1:1 ratio was added. The mixture underwent ultrasonication for 15 min, followed by stirring at room temperature for 24 h. The final composition was collected and labeled as Pt-XTPBPY-CN.

TPBPY-CN-AF: Ex-situ synthesized TPBPY-CN is synthesized by mixing specific quantity of TP-BPY-COF and g-C_3N_4. Then, the mixture was evacuated after three freeze–pump–thaw cycles and heating at 120 °C for 72 h. The final samples were labelled as XTPBPY-CN-AF (where X represents the mass fraction of TP-BPY-COF).

2.2. Catalyst characterization

To provide a comprehensive understanding of the synthesized catalysts, an array of analytical techniques was employed to investigate their structural, morphological, and electronic properties. The characterization encompassed:

X-ray Diffraction (XRD) Analysis: The crystal structure was probed using a Bruker D8 Advance X-ray diffractometer.

Scanning Electron Microscopy (SEM): Surface morphology was examined with a ZEISS Sigma 500 instrument (Japan).

High-Resolution Transmission Electron Microscopy (HRTEM): Microstructure was detailed using a JEOL JEM-2100F microscope (Japan).

X-ray Photoelectron Spectroscopy (XPS): Surface chemical states and electronic configurations were analyzed through a Thermo K-alpha spectrometer (USA). XPS spectra were meticulously calibrated using the C 1 s peak at 284.6 eV derived from the adventitious carbon surface.

Ion Chromatography (IC): Thermo ICS 1100 Ion chromatography was used to analyze the adsorbed ion on the surface of used photocatalyst (USA).

Electron Paramagnetic Resonance (EPR) Spectroscopy: Electron spin resonance properties were explored using a Bruker A300 instrument (Germany).

UV–Vis Diffuse Reflectance Spectroscopy (UV–Vis-DRS): Optical characteristics were assessed with a Shimadzu UV-3600 + spectrophotometer (Japan).

Photoluminescence Spectrum (PL): Photoluminescent behavior was investigated employing a HITACHI F-4600 spectrophotometer (Japan).

The Pt XAFS measurements were performed with Si (1 1 1) crystal monochromators at the BL14W Beam line at the Shanghai Synchrotron Radiation Facility (SSRF) (Shanghai, China). Before the analysis at the beamline, samples were placed into aluminum sample holders and sealed using Kapton tape film. The XAFS spectra were recorded at room temperature using a 4-channel Silicon Drift Detector (SDD) Bruker 5040. Pt L_3-edge extended X-ray absorption fine structure (EXAFS) spectra were recorded in transmission/fluorescence mode. Negligible changes in the line-shape and peak position of Pt L_3-edge XANES spectra were observed between two scans taken for a specific sample. The XAFS spectra of these standard samples were recorded in transmission mode. The spectra were processed and analyzed by the software codes Athena. The EXAFS contributions were separated from different coordination shells by using a hanning windows (dk = 1.0 Å-1). Subsequently, the quantitative curve-fittings were carried out in the R-space (1.0–2.1 Å) with a Fourier transform k-space range of 3.0–12 $Å^{-1}$ using the module ARTEMIS of IFEFFIT. During the curve-fitting, the overall amplitude reduction factor S_0^2 was fixed to the best-fit value of 1.0 determined from fitting the data of metal Pt foil. For the sample, the structural parameters, such as the coordination number N, interatomic distance R, the Debye-Waller factor σ^2 and the edge-energy shift ΔE_0 were allowed to vary during the fitting process.

2.3. Catalyst evaluation

The catalytic performance of the synthesized catalysts for the photocatalytic oxidation of NO was evaluated within a continuous flow cube reactor. This reactor, constructed from quartz, was entirely enclosed in aluminum foil, except for the top surface, and featured dimensions measuring 20 × 15 × 10 cm. Before each experiment, 0.2 g of the prepared catalysts were dispersed in 15 mL of deionized water and underwent ultrasonication for 15 min. Following this, the resulting mixture was deposited into a glass dish with a diameter of 12 cm and then dried under vacuum at 60 °C for a duration of 6 h. After this drying process, the glass dish was centrally positioned within the cube reactor. The onset of the photocatalytic reaction was triggered by the vertical placement of a 300 W Xenon lamp. This high-intensity lamp was thoughtfully fitted with a 420 nm cutoff filter and situated at a precise distance of 20 cm above the catalyst surface. The photocatalytic oxidation of NO commenced upon reaching an adsorption–desorption equilibrium between NO and the catalyst. Throughout the catalytic reaction, a 50 ppm concentration of NO, obtained from a compressed gas cylinder while maintaining N_2 equilibrium was methodically diluted with pure air to achieve a precisely controlled final concentration of 800 ppb. This gas mixture was subsequently directed over the catalyst's surface within the reactor. The total flow rate within the reactor was consistently maintained at 2 L/min. Over the entire duration of the reaction, the concentrations of both NO and NO_2 were diligently monitored and systematically recorded with the assistance of a NO_x analyzer (API-T200, USA). This state-of-the-art instrument allowed for precise and real-time measurement of gas concentrations. To quantify the photocatalytic efficiency of NO removal, the following equation was employed:

$$\varphi = \frac{C_0 - C}{C_0} \times 100\% \quad (1)$$

Here, C0 (in ppb) represented the initial concentration of NO at the commencement of the reaction, while C (in ppb) denoted the concentration of NO at a specific time during the reaction.

2.4. Electrochemical measurements

Electronic properties were evaluated via electrochemical impedance spectroscopy (EIS) and transient photocurrent (TPC) response measurements. The experimental setup consisted of a conventional three-electrode system utilizing a CHI660E electrochemical workstation from Shanghai Chenhua, China. Here, the photocatalyst served as the working electrode, the Pt electrode functioned as the counter electrode, and the Ag/AgCl electrode served as the reference electrode. Preparation of the working electrode involved suspending 10 mg of the catalyst in 1 mL of DI water/ethanol, with the addition of 50 μL of Nafion ethanol solution, followed by 30 min of sonication to ensure a homogeneous suspension. This suspension was then applied onto an FTO glass substrate and allowed to dry at room temperature under the influence of an infrared lamp. For the experimental conditions, a 300 W xenon lamp provided the visible-light source, and a 0.1 mol/L Na_2SO_4 solution served as the electrolyte during photocurrent response experiments, EIS, and Mott-Schottky tests.

2.5. Active species trapping experiment

In a quest to unveil the distinct roles of various active species in the photocatalytic oxidation of NO, an active species trapping experiment was conducted. Specifically, potassium iodide (KI), potassium dichromate ($K_2Cr_2O_7$), *tert*-butanol (TBA), and p-benzoquinone (PBQ) were employed as reagents to capture h^+, e^-, •OH, and $•O_2^-$, respectively.

2.6. In-situ DRIFTs

In-situ diffuse reflectance infrared Fourier transform spectroscopy (DRIFTS) was performed on a INVENIO S spectrometer (Bruker, Germany). Firstly, the samples were pre-treated by heating 1 h at 90 °C to remove the adsorbed gases on the surface of samples. Secondly, 100 mL/min NO/Air mixture gases (800 ppb NO) were introduced into the sample cell and recorded the DRIFTS curve in darkness for 30 min. Lastly, turned on the light source (300 W, Xenon light) with 420 nm cutoff filter, recorded the DRIFTS result per 5 min during illumination.

2.7. DFT calculation details

We used the DFT (Density Functional Theory) as implemented in the Vienna Ab initio simulation package (VASP) in all calculations. The

exchange–correlation potential is described by using the generalized gradient approximation of Perdew-Burke-Ernzerhof (GGA-PBE). The projector augmented-wave (PAW) method is employed to treat interactions between ion cores and valence electrons. The plane-wave cutoff energy was fixed to 450 eV. Given structural models were relaxed until the Hellmann–Feynman forces smaller than −0.02 eV/Å and the change in energy smaller than 10^{-5} eV was attained. Grimme's DFT-D3 methodology was used to describe the dispersion interactions among all the atoms in adsorption models. Climbing Image Nudge Elastic Band (CI-NEB) method conbined with VTST was used to produce transition states and calculate the energy barrier; to ensure the accuracy of transition states and energy barriers, 6 images were produced and calculated among every two products.

3. Results and discussion

3.1. Crystal phase and Microstructure

The in-situ synthesis of TP-BPY-COF on g-C_3N_4 (CN) was realized through a strategic reaction process where CN was introduced into a solvent mixture containing 1,3,5-Triformylphloroglucinol (TP) and 2,2′-bipyridine-5,5′-diamine (BPY), subsequently subjected to hydrothermal conditions. The process leverages Schiff base reactions, wherein the aldehyde groups of TP react with both the amine groups of BPY to form the COF structure and the amine-rich surface of CN, shown in Fig. 1**(a)**. This dual reaction pathway not only facilitates the formation of the COF but also ensures its in-situ growth on the CN substrate, seamlessly integrating the COF into the composite material. To determine the influence of this in-situ growth technique on the photocatalytic activity, a counterpart composite, ex-situ growth TPBPY-CN-AF, was prepared for comparison. This reference sample was synthesized by mechanically mixing CN with previously synthesized TP-BPY-COF, followed by undergoing the same hydrothermal treatment at 120 °C for three days, aiming to understand the benefits of the in-situ formation approach.

The phase structures of the as-synthesized CN, TP-BPY-COF, TPBPY-CN, and Pt-TPBPY-CN catalysts were systematically examined through powder X-ray diffraction (PXRD) analysis. As depicted in Fig. 1**(b)**, the PXRD patterns of CN exhibited a close alignment with the reference pattern for CN (PDF87-1526#), unequivocally confirming the successful synthesis of a crystalline graphite-like carbon nitride [29]. An observable new peak at 3.6° emerged in the PXRD patterns of TPBPY-CN, corresponding to the (1 0 0) facet of TP-BPY-COF, indicating the formation of TP-BPY-COF during synthesis [30]. Meanwhile, the structure of TP-BPY-COF was also comfirmed, as shown in Fig. 1**(c)**. In the case of Pt-40TPBPY-CN composites, the absence of discernible diffraction peaks assigned to platinum suggests a high dispersion of platinum species, possibly indicative of the formation of single-atom platinum on the surface of TP-BPY-COF. Consequently, these PXRD findings decisively validate the successful synthesis of Pt-TPBPY-CN without compromising the structural integrity of the constituent materials.

The morphological structure and elemental composition of the as-prepared photocatalyst were confirmed through SEM and elemental analysis. Fig. 2**(b)** highlights the distinctive strip-like morphology of TP-BPY-COF, which differs from the prior research using the same synthesis method [31]. This divergence could be attributable to uncontrollable variations in the reaction conditions such as vacuum condition and precursor concentrations, which could have impacted the crystallization process of TP-BPY-COF, suggesting the critical nature of precise control over synthetic parameters to dictate the resultant COF structure. Meanwhile, SEM images of TPBPY-CN (Fig. 2**(d)**) reveal the emergence

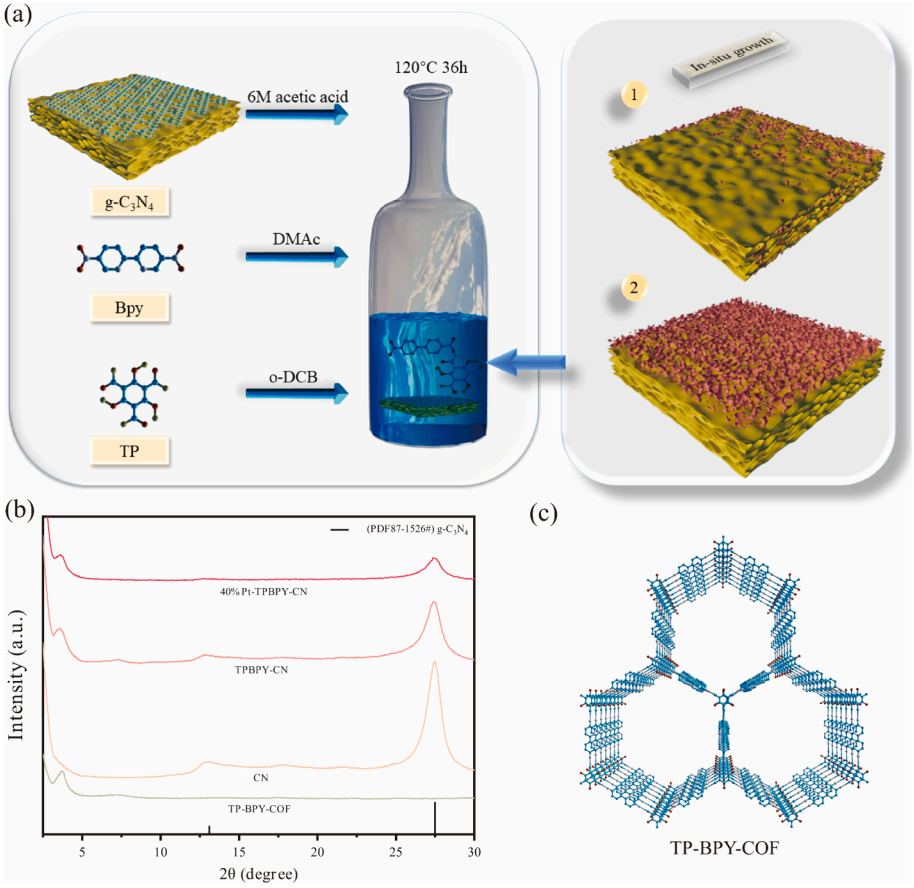

Fig. 1. (a) Schematic representation detailing the synthesis procedure for TPBPY-CN. (b) XRD patterns illustrating the crystalline structures of CN, TP-BPY-COF, TPBPY-CN and Pt-TPBPY-CN and (c) The molecular structure of TP-BPY-COF.

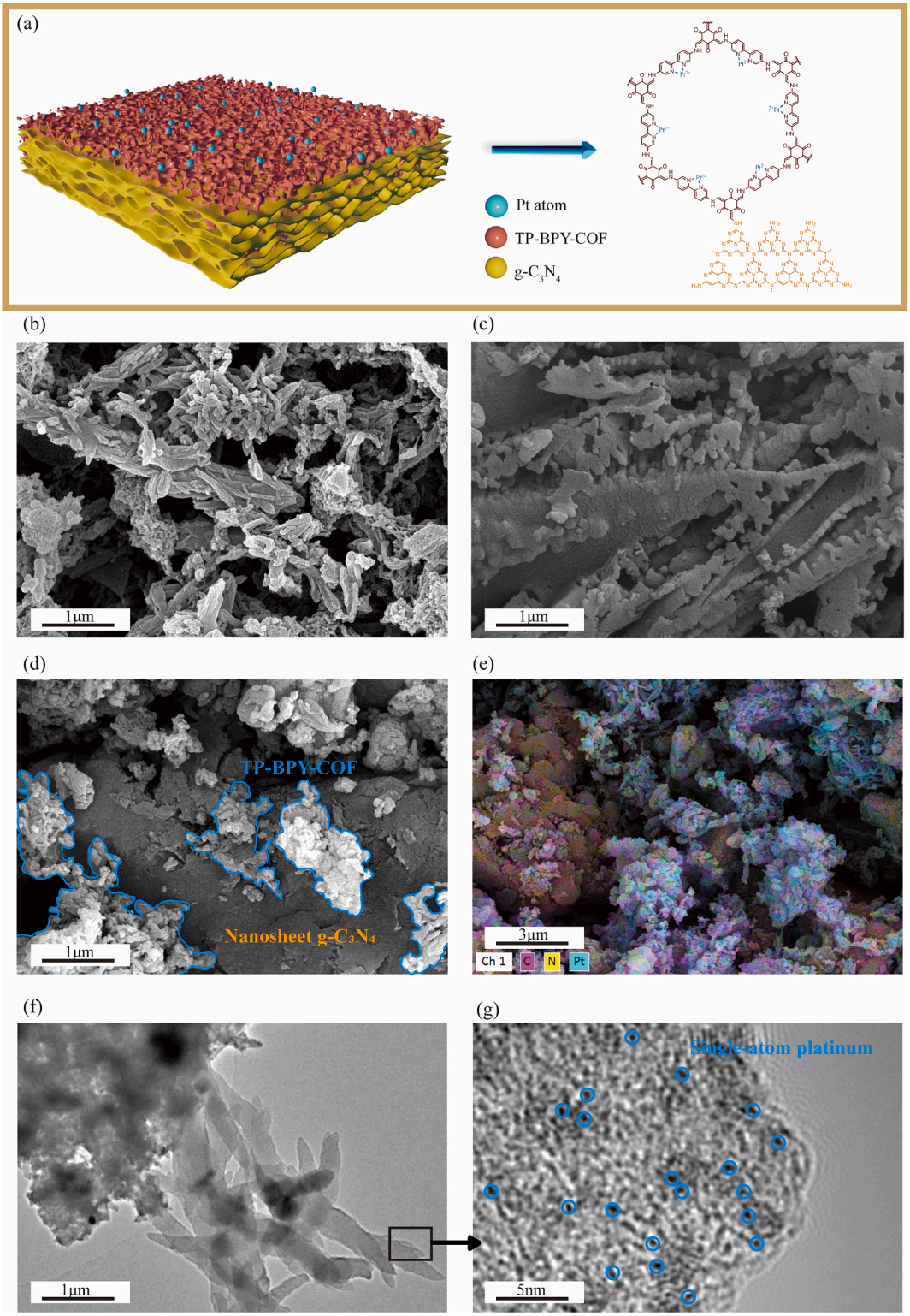

Fig. 2. (a) Molecular structure of Pt-40TPBPY-CN, SEM images of (b) TP-BPY-COF, (c) CN, (d) TPBPY-CN and (e) EDS mapping (f-g) TEM image of Pt-40TPBPY-CN.

of strip-like structures growing on the surface of the nanosheet CN structure (Fig. 2**(c)**), providing clear evidence of the in-situ growth of TP-BPY-COF on the surface of CN during synthesis [32]. In Fig. 2**(e)**, EDS mapping of Pt-TPBPY-CN reveals that platinum is predominantly concentrated on the strip-like structures of TP-BPY-COF, thereby confirming the platinum coordinated on TP-BPY-COF. Moreover, the in-situ growth of strip-like TP-BPY-COF on the nanosheet CN is also evident by TEM results, showed in Fig. 2**(f)**. Upon further investigation of the TP-BPY-COF depicted in Fig. 2**(g)**, it was observed that single-atom platinum exists on strip-like TP-BPY-COF, aligning with the consistent findings of EDS mapping. Based on the XRD, SEM, and TEM results, the morphological and molecular structure of Pt/TP-BPY-CN is briefly illustrated in Fig. 2**(a)**.

3.2. Electronic structure

The XPS analysis was conducted to probe the elemental composition and chemical states of CN, TP-BPY-COF, 40TPBPY-CN and Pt-40TPBPY-CN photocatalysts. High-resolution C 1 s spectra (Fig. 3**(a)**) revealed two prominent peaks in the C 1 s spectra of CN: C-C (284.8 eV) and N-C=N (288.3 eV), respectively [33]. In contrast, the C 1 s spectra of TP-BPY-COF displayed four distinct peaks at 284.8 eV, 286.0 eV, 288.4 eV, and 290.9 eV, corresponding to C-C, C-N, C=O, and π-π excitation, respectively [26]. In the N 1 s spectra (Fig. 3**(b)**) of the as-prepared samples, four distinctive peaks were observed in the N 1 s spectra of CN, corresponding to C=N-C (398.8 eV), N-$(C)_3$ (399.6 eV), C-NH_x (401.3 eV), and π-π excitation (404.2 eV), respectively [34]. Meanwhile, the N 1 s spectra of TP-BPY-COF displayed two peaks at 398.8 eV and 400.1 eV, attributed to C=N-C and C-N bonds [35]. After integration of TP-BPY-COF and CN, it was observed that the peaks belonging to TP-BPY-COF dominated the N 1 s spectra of 40TPBPY-CN, with only the peak related to C-NH_x bond (401.3 eV) remaining on the 40TPBPY-CN sample. This confirms that TP-BPY-COF is in-situ grown on the surface of CN through a Schiff base reaction between the C-NH_x of CN and the H-C=O of TP-BPY-COF, which obscures the CN peaks except for the C-NH_x bond. According to both C 1 s and N 1 s spectra, the peaks corresponding to C-N bonds of TP-BPY-COF shifts towards higher binding energies after incorporating platinum, indicating the electron transfer from TP-BPY-COF to platinum.

3.2.1. In-situ XPS analysis

In-situ XPS experiments were carried out to investigate electron interactions between CN, TP-BPY-COF, and platinum during photocatalytic reactions [36]. To accurately simulate the photocatalytic reaction conditions during activity measurement experiments, in-situ XPS experiment were conducted under four distinct sets of conditions: in the dark without NO exposure, under illumination without NO, in the dark with NO present, and under illumination with NO. As shown in Fig. 3**(c)**, a noteworthy observation was the discernible shift in the binding energy of the C=O peak (288.4 eV) of TP-BPY-COF toward lower energy levels during illumination. This phenomenon signifies the effective transfer of photogenerated electrons to TP-BPY-COF, thereby rendering it electron-rich. Simultaneously, in the in-situ high-resolution N 1 s spectra (Fig. 3**(d)**), a substantial shift was recorded in the binding energy of the C-NH_x (401.3 eV) bond, which displayed an increase of 0.23 eV during the presence of light. This shift provides compelling evidence of the transfer of photogenerated electrons from the C-NH_x bond of CN to the C=O bond of TP-BPY-COF during photocatalytic reaction. Specifically, electrons transfer from CN to TP-BPY-COF through the −H-C-N-H- bond, formed via a Schiff base reaction between the additional C-NH_2 of CN and the extra H-C=O of TP-BPY-COF.

In the Pt 4f spectra (Fig. 3**(e)**), two prominent peaks were discerned at binding energies of 72.3 eV and 75.7 eV, ascribed to the 4f 7/2 and 4f 5/2 states of $Pt^{\delta+}$, respectively [37]. However, it was notable that these Pt peaks exhibited a marginal shift towards lower binding energies under illumination, providing compelling evidence of electron transfer from TP-BPY-COF to platinum, facilitated by plasmonic resonance [38]. Furthermore, it was evident that the peaks shifted towards higher binding energy under NO atmosphere, indicating the transfer of electrons from platinum to adsorbed NO gases during the photocatalytic reaction. Notably, two new peaks emerged at binding energies of 74.8 eV and 78.4 eV, corresponding to the 4f $_{7/2}$ and 4f $_{5/2}$ states of Pt^{4+}, when subjected to light in the presence of NO gas. Simultaneously, the peak associated with $Pt^{\delta+}$ underwent a shift towards higher binding energy, indicating an increased valence state of $Pt^{\delta+}$. These outcomes substantiate the oxidation of $Pt^{\delta+}$ under both illumination and nitric oxide atmosphere, attributed to the sequential electron transfer from $Pt^{\delta+}$ to nitric oxide. Moreover, it is important to note that the inclusion of platinum introduced a novel NO reduction pathway during the photocatalytic reaction.

3.2.2. EXAFS and XANES

Extended X-ray Absorption Fine Structure (EXAFS) and X-ray Absorption Near-Edge Structure (XANES) analysis were conducted to delve into the local coordination and electronic structure of individual platinum atoms in the Pt-40TPBPY-CN sample [39]. The XANES spectra at the Pt L_3-edge (Fig. 4**(a)**) reveal that the white line peak for Pt-40TPBPY-CN lies between those of PtO_2 and Pt foil, indicative of platinum's

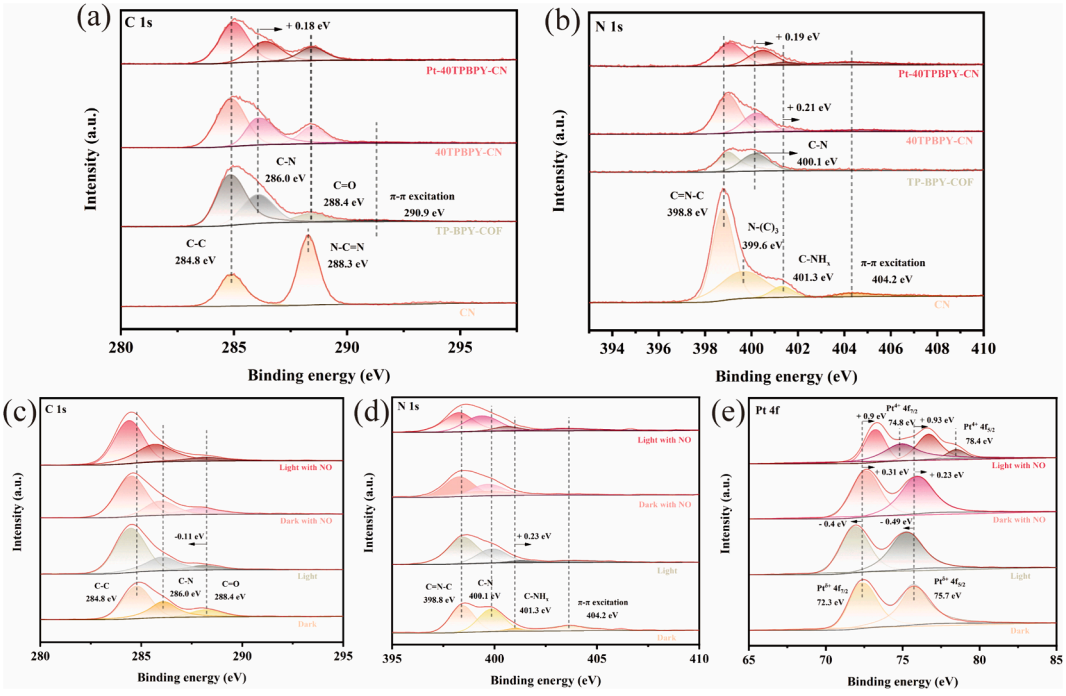

Fig. 3. The XPS spectra of CN, TP-BPY-COF, 40TPBPY-CN and Pt-40TPBPY-CN photocatalysts (a)C 1 s spectra. (b)N 1 s spectra. The in-situ XPS spectra of CN, TP-BPY-COF, 40TPBPY-CN and Pt-40TPBPY-CN photocatalysts (c) C 1 s spectra. (d) N 1 s spectra. (e) Pt 4f spectra.

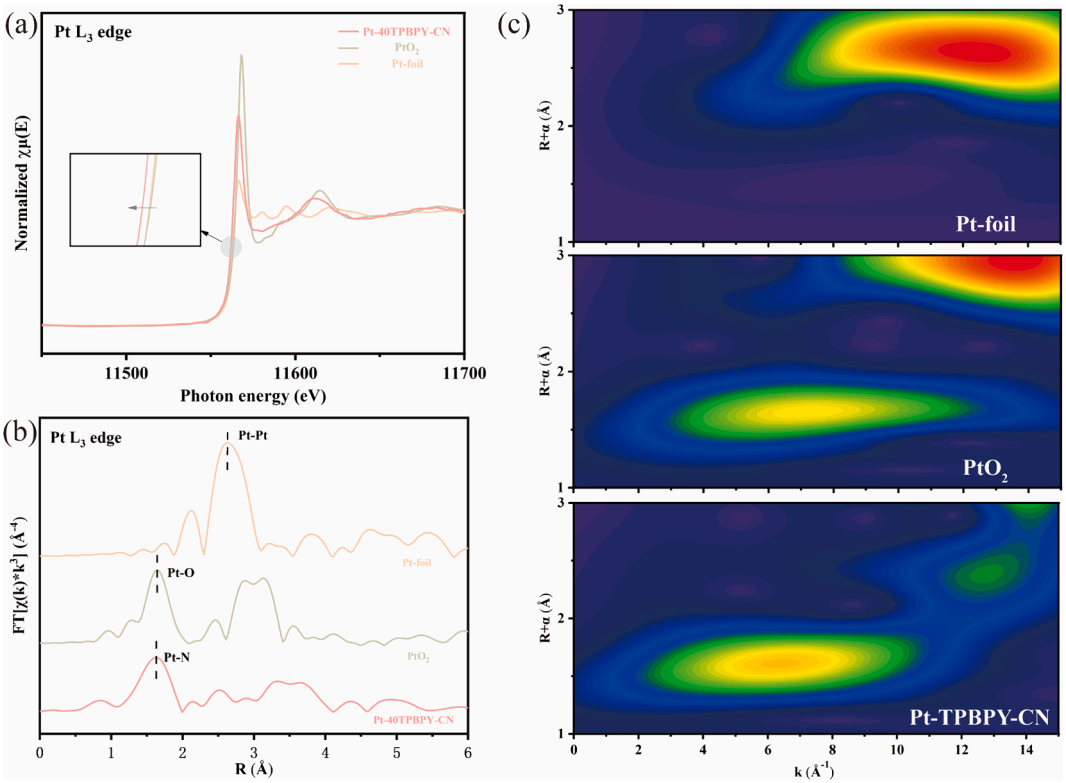

Fig. 4. (a) Pt L_3-edge XANES, (b) k_3-weighed Pt L_3-edge FT-EXAFS spectra in the R space and (c) Pt L_3-edge WT-EXAFS plots of TP-BPY-COF, PtO_2 and Pt foil.

oxidation state ranging from 0 to + 4 in Pt-40TPBPY-CN, consistent with XPS findings.

The Pt L_3-edge EXAFS Fourier Transform (FT) spectra in Fig. 4**(b)** exhibit a predominant peak at 1.63 Å for the Pt-40TPBPY-CN sample, attributed to Pt-N coordination [40]. Conversely, PtO_2 and Pt foil spectra showcase prominent peaks at 1.64 and 2.63 Å, corresponding to

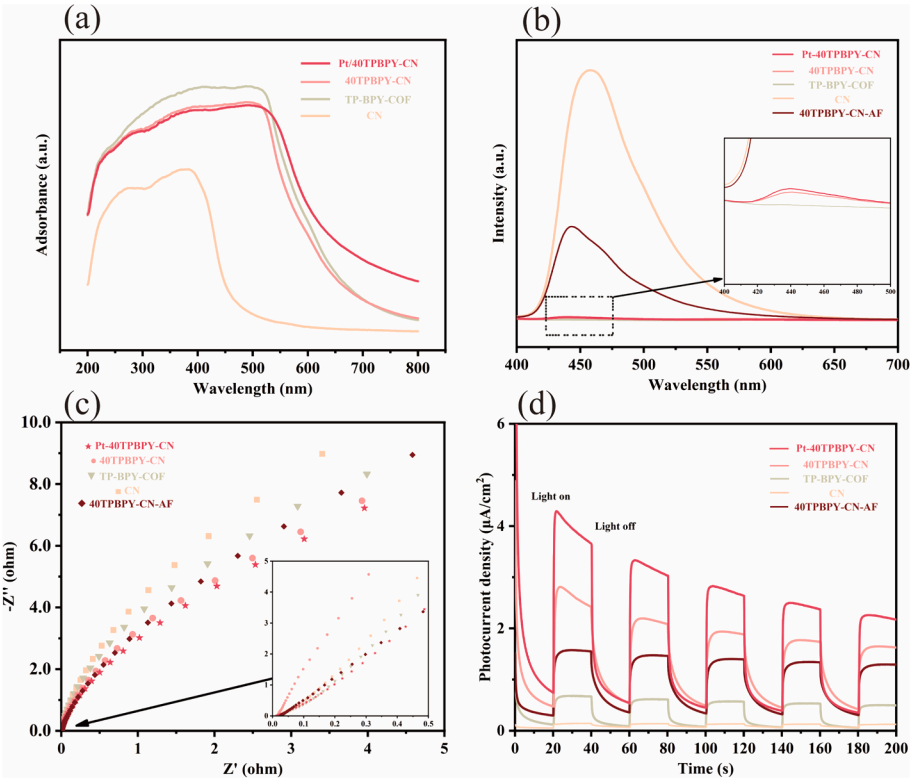

Fig. 5. (a) UV–vis DRS spectra, (b) PL spectra, (c) EIS Nyquist plots, (d) transient 437 photocurrent response curves of CN, TP-BPY-COF, TPBPY-CN, Pt-40TPBPY-CN and 438 40TPBPY-CN-AF photocatalysts.

Pt-O and Pt-Pt coordination, respectively. Despite the proximity of the Pt-N peak to Pt-O, further confirmation of Pt-N coordination is obtained through the fitting of FT EXAFS curves, as depicted in **Fig. S1**, where the notable peak at 2.03 Å is assigned to the Pt-N bond. Additionally, the fitting results in **Table S1** reveal a coordination number of 6.6 for Pt-N, indicating coordination with six nitrogen atoms.

Wavelet-Transform (WT) EXAFS analysis presents WT contour plots of the three k^3-weighted $\chi(k)$ signals based on Morlet wavelets with optimal resolution (Fig. 4**(c)**). Pt-40TPBPY-CN exhibits a WT maximum with a k value of 6.2 $Å^{-1}$, less than that of PtO_2, further confirming the presence of the Pt-N path in Pt-40TPBPY-CN. Furthermore, the maximum WT intensity of Pt foil is positioned at 12.5 $Å^{-1}$, corresponding to the Pt-Pt path [41]. In conclusion, the combined EXAFS and XANES results affirm the 0 to + 4 oxidation state of the Pt atom, existing singularly and coordinating with nitrogen atoms in Pt-40TPBPY-CN.

3.3. Photoelectrochemical properties and band structures

The electronic structure and photoelectrochemical characteristics of the prepared samples were further elucidated through the analysis of UV–vis DRS and PL spectroscopy [42]. In the UV–vis DRS spectra (Fig. 5 **(a)**), TP-BPY-COF exhibited substantial light absorption intensity in the visible light spectrum, significantly enhancing the light absorption of 40TPBPY-CN across both the ultraviolet and visible ranges. Moreover, the introduction of platinum further augmented visible light absorption, resulting in the highest visible light absorption intensity among the synthesized samples. Fig. 5**(b)** illustrates the PL spectra of the synthesized photocatalysts, excited at a 370 nm emission wavelength under room temperature conditions. Notably, the peaks associated with CN and 40TPBPY-CN-AF photocatalysts displayed relatively high peak intensities, indicating a high recombination rate between photogenerated electrons and holes. For the TP-BPY-CN and 40TPBPY-CN samples, there was an almost negligible peak intensity at 460 nm, affirming that TP-BPY-COF possesses strong performance to inhibit the recombination of photogenerated electron and holes. In conclusion, the in-situ growth of TP-BPY-COF on the surface of CN effectively suppressed carrier recombination of 40TPBPY-CN photocatalyst.

The efficiency of photogenerated electron and hole transfer is a critical factor influencing photocatalytic performance, and it was evaluated through photocurrent response and EIS. As depicted in Fig. 5**(c)**, the EIS Nyquist plots of the Pt-40TPBPY-COF sample exhibited the lowest electrochemical impedance, indicating rapid charge transfer during photocatalytic reactions [43]. Additionally, transient photocurrent response curves (Fig. 5**(d)**) showed that Pt-40TPBPY-CN exhibited the highest photocurrent density, approximately 5-fold and 3-fold greater than that of CN and TP-BPY-COF, respectively. Consequently, the combination of TP-BPY-COF and CN significantly enhances the photoelectrochemical properties by accelerating the transfer rate of electrons and holes, while simultaneously inhibiting their recombination. In addition, the incorporation of platinum onto TP-BPY-COF further enhances these capabilities. To further explore the photocatalytic reaction mechanism, the band structures of Pt/40TPBPY-CN were obtained by both M−S plots and XPS-VB analysis, detailed in **Text S2**.

To investigate the impact of in-situ growth on the catalytic performance, we conducted a comparative analysis of the photoelectrochemical properties between in-situ grown catalysts and ex-situ synthesized catalysts. It is evident that 40TPBPY-CN exhibits superior photoelectrochemical properties compared to 40TPBPY-CN-AF, as indicated by the lower recombination rate of electron/hole pairs, lower electrochemical impedance, and higher photocurrent density. These results confirm that chemically bonded photocatalytic materials can significantly enhance photocatalytic performance.

3.4. Photocatalytic performance of NO degradation

Catalytic activity tests were conducted to assess the photocatalytic efficiency of NO removal using the prepared samples. Fig. 6**(a)** illustrates the photocatalytic efficiency for varying mass fractions of TPBPY-CN, demonstrating an enhancement in efficiency with an increased mass fraction ratio of TP-BPY-COF. Notably, when the mass fraction of TP-BPY-COF exceeded 40 %, the photocatalytic performance gradually declined, confirming the attainment of maximum efficiency at 44.8 % when the mass fraction is 40 %. This result underscores the synergistic relationship between CN and TP-BPY-COF, aligned with their photoelectrochemical properties. In addition, the synergistic interaction is mainly induced through in-situ growth, as evidenced by 40TPBPY-CN-AF exhibited only 31.8 % photocatalytic efficiency, which is lower than 40TPBPY-CN. To evaluate the effect of single atom on photocatalytic performance, photocatalytic efficiency of Pt/40TPBPY-CN was analyzed. Fig. 6**(b)** presents an efficiency comparison between Pt/40TPBPY-CN and 40TPBPY-CN. The results clearly indicate a substantial increase in photocatalytic efficiency following the incorporation of platinum with efficiencies of 65 %, confirming a superior photocatalytic composite of TPBPY-CN for single atom doping. Consequently, Pt/40TPBPY-CN demonstrates the highest photocatalytic efficiency, better than other reported photocatalysts (**Table S2**). Meanwhile, the first-order reaction rate (**Fig. S3**) of Pt/40TPBPY-CN (0.1580 min^{-1}) was 5.47, 2.78 and 1.99 times that of CN (0.0289 min^{-1}), TP-BPY-COF (0.0569 min^{-1}) and 40TPBPY-CN (0.0793 min^{-1}), respectively. Furthermore, Pt/40TPBPY-CN exhibited nearly 100 % NO_3^- oxidation selectivity (Fig. 6**(c)**), while 40TPBPY-CN and CN achieved NO_3^- oxidation selectivity of 97.9 % and 89 %, respectively, confirming the superior selectivity of Pt/40TPBPY-CN samples. The remarkable photocatalytic performance could be induced by the formation of chemically bonded heterostructure which facilitates the acceleration of photogenerated e^-/h^+ transfer and attenuation of their recombination. In addition, single atom Pt also played a critical role during the photocatalytic reaction due to the additional electrons provided by surface plasmon resonance (SPR). Moreover, 600-minute cycle tests were conducted to evaluating the stability of the prepared photocatalysts, depicting the results in Fig. 6**(d)**. It is evident that the efficiency of Pt/40TPBPY-CN decreased from 63 % to 59 % after five cycle experiments, indicating good stability during the photocatalytic reaction. Moreover, the PXRD patterns of 40Pt-TPBPY-CN photocatalyst after reaction (**Fig. S4**) demonstrated the almost same peak as the pristine catalysts, further confirming the stability of 40Pt/TPBPY-CN.

3.5. Mechanism of simultaneously photocatalytic oxidation and reduction of NO

3.5.1. Evaluation of ROS

The electron paramagnetic resonance (EPR) experiments with 5,5-dimethyl-1-pyrroline N-oxide (DMPO) were conducted to further investigate the production of •OH and $•O_2^-$ species during the photocatalytic reaction. Fig. 7**(a) and (b)** illustrate the peak intensities of •OH and $•O_2^-$ for the prepared samples, respectively. Comparatively, TP-BPY-COF exhibited a stronger •OH EPR signal than CN, whereas CN displayed a greater ability to produce $•O_2^-$ than TP-BPY-COF. However, 40TPBPY-CN exhibited stronger •OH and $•O_2^-$ EPR signals than TP-BPY-COF and CN, further confirming the synergistic effect between TP-BPY-COF and CN in enhancing the production of •OH and $•O_2^-$ radicals during photocatalytic reactions. Additionally, Pt/40TPBPY-CN demonstrated the strongest peak signals in both •OH and $•O_2^-$ EPR spectra, indicating increased photogenerated electron production under visible light illumination.

Active species trapping experiments were conducted to assess the impact of individual active species during the photocatalytic degradation of NO. As illustrated in Fig. 7**(c)**, it is evident that e^- play the most crucial role in the photocatalytic reaction, given that the sample

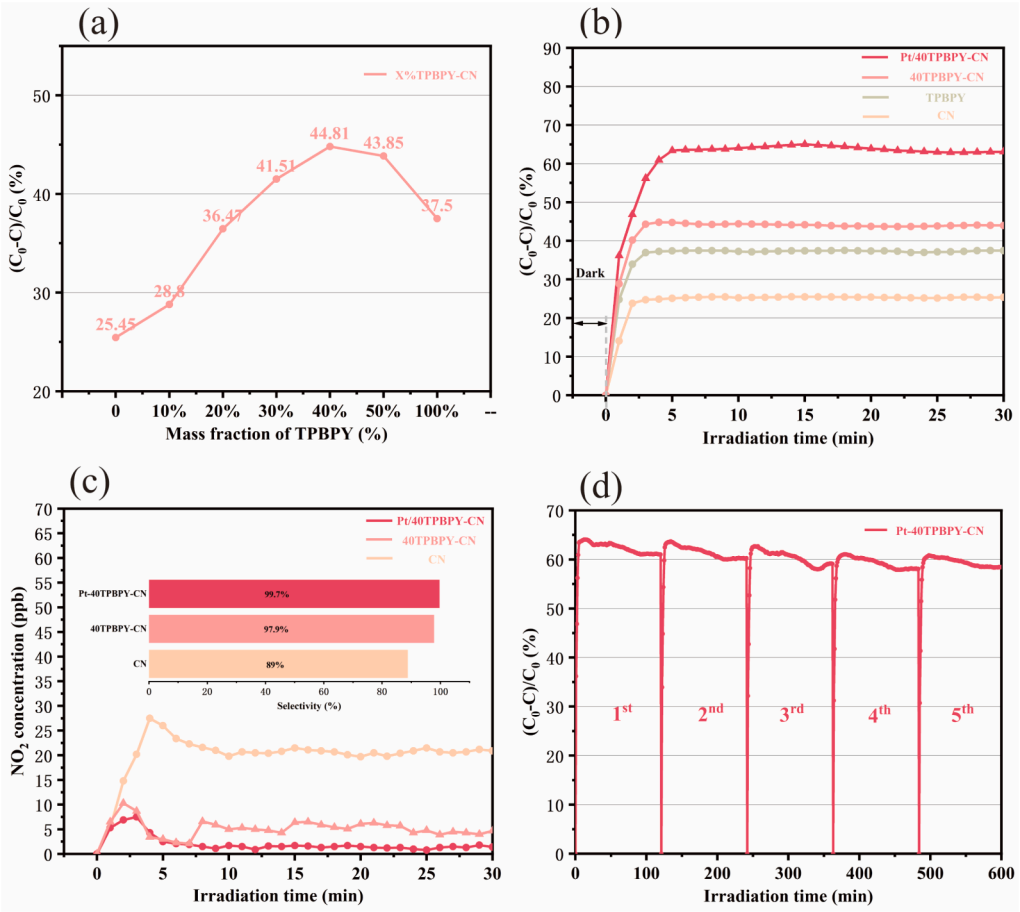

Fig. 6. (a) Photocatalytic removal efficiency of NO for 0/10/20/30/40/50/100 TPBPY-CN, (b) Photocatalytic removal efficiency of NO for CN, TP-BPY-COF, 40TPBPY-CN, Pt/40TPBPY-CN and 40TPBPY-CN-AF (c) the selectivity of NO for CN, 40TPBPY-CN and Pt/40TPBPY-CN and (d) 600 mins cycle experiment result of Pt/40TPBPY-CN.

trapping e^- demonstrated the lowest photocatalytic efficiency. Additionally, $\bullet O_2^-$ emerges as a primary active oxidizing species, as indicated by a photocatalytic efficiency of 13.5 % during trapping experiments. Comparatively, holes (h^+) and hydroxyl radicals (•OH) exhibit a relatively lower impact on photocatalytic performance, retaining 32.1 % and 41.5 % photocatalytic efficiency, respectively. These results collectively conclude that e^- are the most crucial active species in this photocatalyst. Furthermore, the substantial impact of $\bullet O_2^-$ provides strong evidence that the oxidation reaction constitutes the predominant pathway for NO degradation. This is due to the acknowledged role of $\bullet O_2^-$ as a crucial oxidizing species in the photocatalytic oxidation of NO.

3.5.2. *Theoretical calculation analysis*

In order to delve deeper into the mechanism underlying the complex composition of synthesized photocatalysts, we conducted a comprehensive charge density analysis of Pt/40TPBPY-CN. The charge density difference, depicted in Fig. 7**(d)**, is mathematically expressed as:

$$\rho_{\text{Charge density difference}} = \rho_{C}\text{-}\rho_{g\text{-}C_3N_4}\text{-}\rho_{\text{TP-BPY-COF}}\text{-}\rho_{Pt^{2+}} \quad (2)$$

where ρ represents the charge density. This calculation was aiming to illuminate the electronic interactions and charge redistribution consequent to the integration of CN, TP-BPY-COF and single-atom platinum. From Fig. 7**(d)**, an obvious electron density accumulation, primarily observed near Pt^{2+}, indicating an elevation in the electron density around Pt^{2+}. Conversely, the electron density depletion, predominantly on TP-BPY-COF, confirming a loss of electrons within this component. These observations suggest that electrons are likely to migrate from TP-BPY-COF to Pt^{2+}, thereby rendering Pt^{2+} as a catalytically active site for NO reduction and TP-BPY-COF as a facilitator for NO oxidation. The presence of single atom Pt facilitates a redistribution of electron density greatly contributes to both the reductive and the oxidative process by inducing the electrons transfer from TP-BPY-COF to Pt^{2+}, which is also in great accordance with the in-situ XPS analysis and Bader charge analysis (Table S3).

To further elucidate the promotional effects of Pt/TPBPY-CN on the adsorption and photocatalytic conversion of NO, comprehensive calculations were performed to analyze the adsorption behavior of NO on the catalyst's surface and the evolution of surface species during the reaction. The adsorption energy calculations revealed that NO could simultaneously bind to the Pt^{2+} and carbon atom within the −H-N-C-H- moiety, with adsorption energies of −1.559 eV and −2.013 eV, respectively. This suggests that NO can be readily adsorbed and subsequently catalyzed at these two active sites on Pt/TPBPY-CN. Therefore, we investigated the free energy changes associated with NO oxidation and reduction at these sites, aiming to uncover the preferred reaction pathways from a thermodynamic standpoint. The optimized structure for NO oxidation on the carbon atom, presented in Fig. 8**(b-g)**, shows initial linkage of NO with carbon atom on the −H-N-C-H- bond. Then, O_2 adsorption on the photocatalyst's surface was simulated to be considered as oxidative species, confirmed by trapping experiment. Notebly, O_2 was found to bind to both Pt^{2+} and TP-BPY-COF, suggesting that photogenerated electrons on both Pt^{2+} and TP-BPY-COF can activate O_2, thereby synegistically producing more $\bullet O_2^-$. This result is corroborated by EPR results, indicating a higher $\bullet O_2^-$ signal for Pt/40TPBPY-CN compared to 40TP-BPY-CN. Following the generation of $\bullet O_2^-$, the Pt-O and Pt-N bonds are disrupted, facilitating the attachment of $\bullet O_2^-$ to an

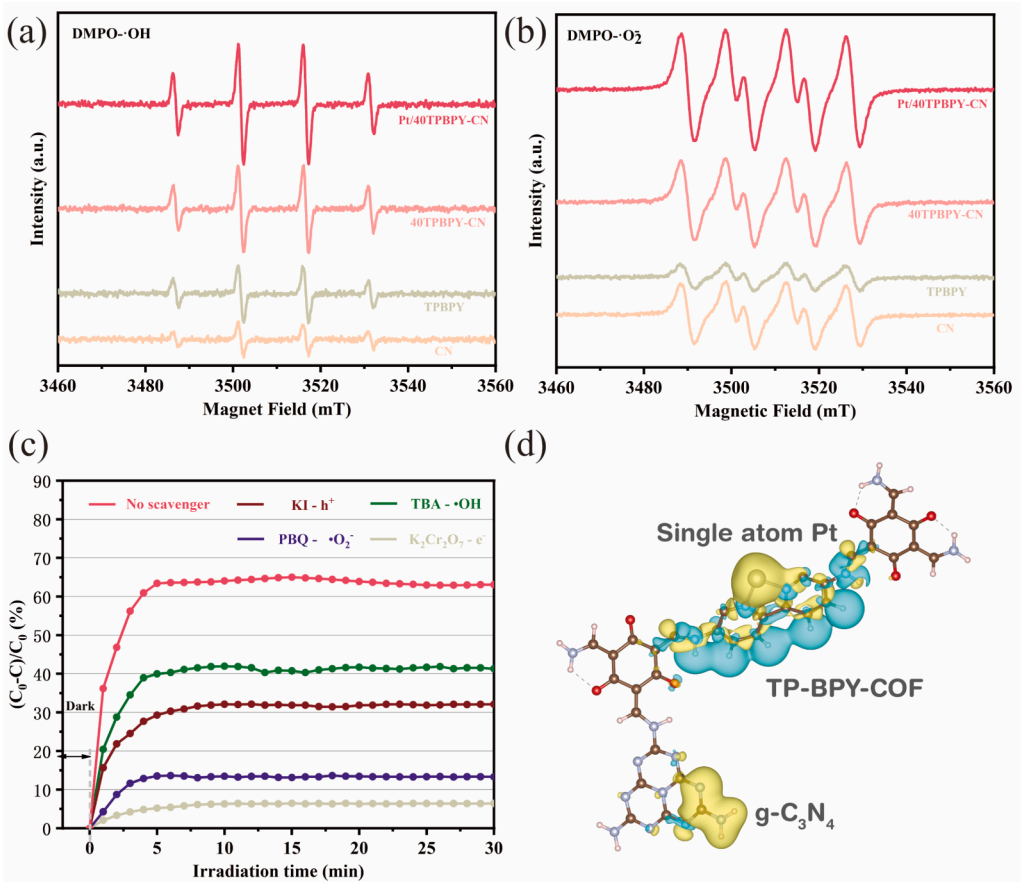

Fig. 7. Intensity of •OH (a) and $•O_2^-$ (b), (c) trapping experiment result of 40Pt/TPBPY-CN, (d) Charge density difference of optimized Pt/TPBPY-CN.

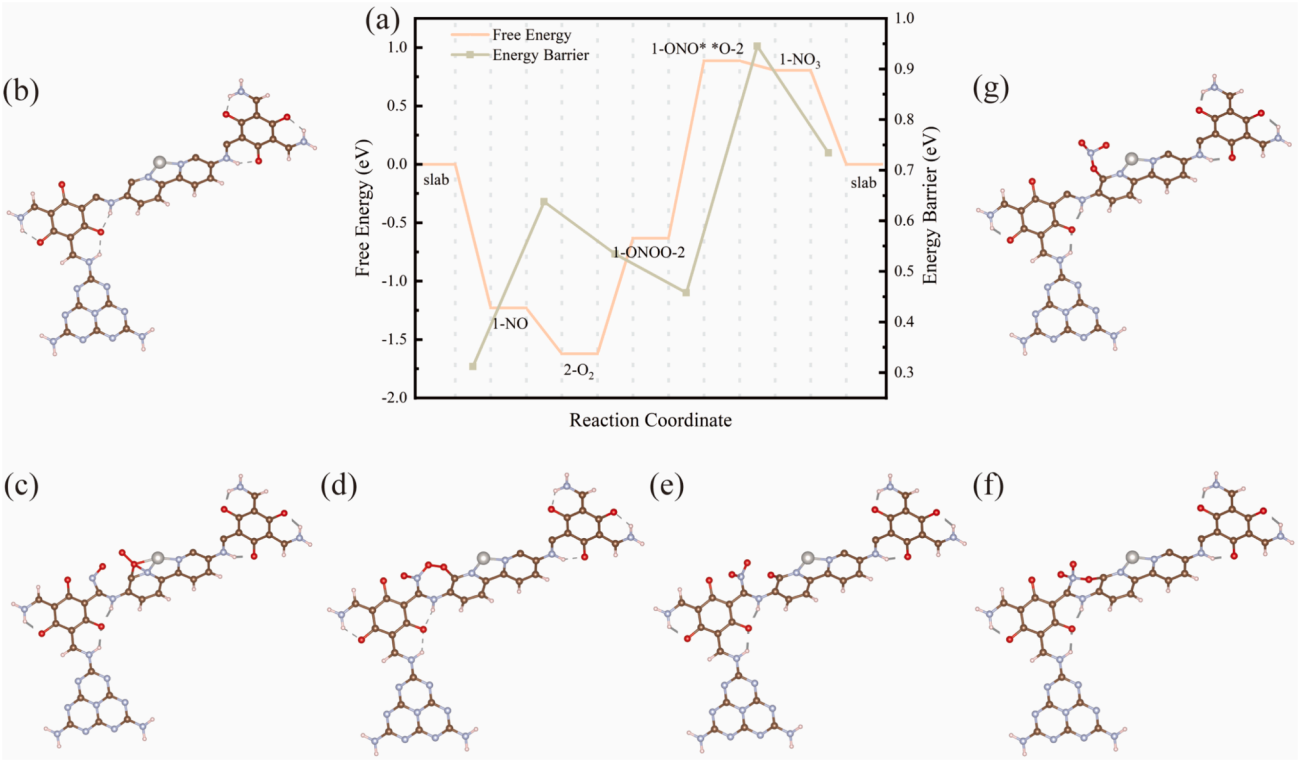

Fig. 8. (a) Free energy and energy barrier of NO oxidation pathway on C atom, (b-g) Optimized structure for NO oxidation on C atom.

adjacent NO molecule, oxidizing it to NO_3^-. Fig. 8**(a)** outlines the free energy changes and the energy barrier during NO oxidation on TP-BPY-COF. The energy barrier is determined as:

$$\Delta E \text{ energy barrier} = E_1 - E_{\text{transition state}} \quad (3)$$

where E_1 represents the energy prior to the transition state, and $E_{\text{transition state}}$ denotes the energy of the state as determined by the CI-NEB method. From Fig. 8**(a)**, it is evident that NO and O_2 are readily adsorbed on the surface, as indicated by the negative △G. However, the free energy for the NO→NO_2*→NO_3* transition increases by 1.05 eV and 1.55 eV, respectively, highlighting the light energy required for these steps and the formation of $\bullet O_2^-$ by photogenerated electrons. Throughout these processes, the formation of NO_3^- presents the highest energy barrier, at 0.94 eV, confirming it as the rate-limiting step.

In our investigation into the reduction pathways of NO adsorbed on Pt^{2+}, we identified a two-step reduction process leading from NO to N_2, and subsequently from N_2 to NH_3, as depicted in Fig. 9**(c-n)**. Initially, NO receives photogenerated electrons from the coordinated Pt^{2+}, facilitating the participation of H^+ in the reduction reaction to form N*. Subsequently, additional NO molecules adsorb onto N* and are reduced to N_2. Notably, the desorption energy barrier for N_2, identified as 0.697 eV (Fig. 9**(a-b)**), exceeds the energy barrier for further reduction to N-NH (0.202 eV), prompting the preferential reduction of N_2 to NH_3 over its desorption from Pt^{4+}. This pathway is corroborated by the stronger competitive adsorption capability of NO (−1.559 eV) compared to N_2 (−0.124 eV), indicating that the majority of the produced NH_3 originates from the initially adsorbed NO. Within this reduction pathway, the desorption of NH_3 emerges as the rate-limiting step, characterized by the highest energy barrier of 1.098 eV. When comparing the energy barriers of NO oxidation and reduction, it becomes evident that NO oxidation predominantly proceeds through photocatalytic degradation reactions. The relatively higher energy barrier and the increased number of reaction steps in the NO reduction pathway contribute to a lesser proportion of NO reduction products, consistent with trapping experiment result.

3.5.3. *Chemically bonded heterostructure*

This study highlights the pivotal roles of TP-BPY-COF and CN in the photocatalytic degradation of NO. The in-situ growth of TP-BPY-COF on CN via a Schiff-base reaction unveils a novel electron transfer pathway, significantly facilitated by the −H-C-N-H bond. This unique method of material integration, which diverges from the conventional approach of directly loading photocatalytic materials, markedly enhances electron transfer and fosters strong intermolecular interactions. A comparative analysis of the photocatalytic performances of 40TPBPY-CN and 40TPBPY-CN-AF reveals that the enhanced interfacial synergy, resulting from chemical bond formation, significantly augments the photocatalytic efficacy observed in this study.

3.5.4. *Bifunctional single-atom platinum*

The unique role of single-atom platinum also emerges as a critical factor in the photocatalytic degradation pathway of NO. This novel bifunctional platinum not only further enhances the production of $\bullet O_2^-$, but also features a redox cycle involving Pt^{2+}/Pt^{4+}, playing a crucial role in facilitating NO reduction. A notable aspect of this process is the transition of platinum's oxidation state from + 2 to + 4 during the photocatalytic reaction, highlighting its dynamic involvement in the mechanism. To gain deeper insights into platinum's function, we conducted an in-depth in-situ XPS experiment. The experimental setup involved subjecting the sample to a 30-minute analysis under light exposure within a controlled NO atmosphere, followed by a subsequent 30-minute period under dark conditions. The results, illustrated in Fig. 10**(a)**, demonstrate the oxidation of platinum from + 2 to + 4 states

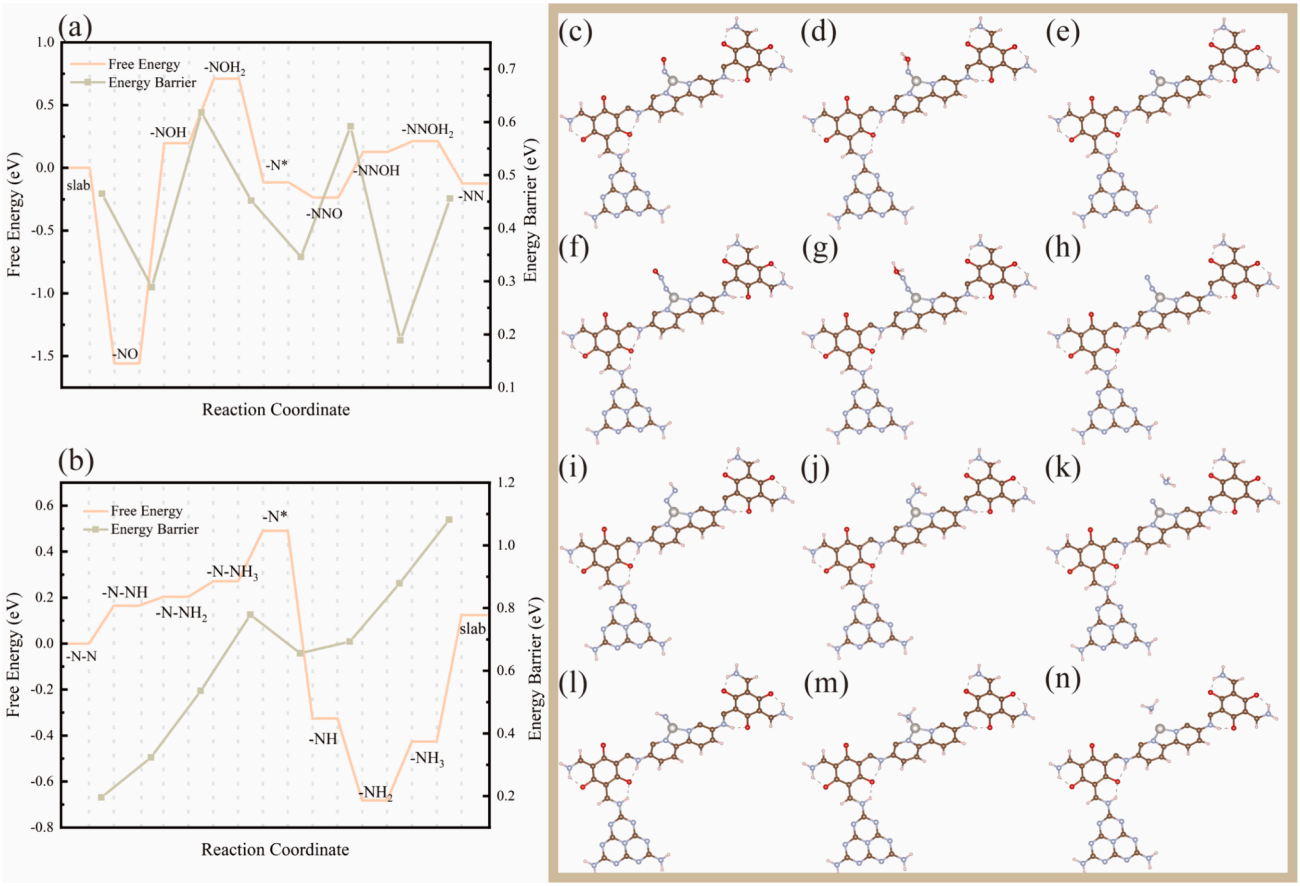

Fig. 9. (a-b) Free energy and energy barrier of NO reduction pathway on Pt^{2+}, (c-n) Optimized structure for NO reduction on Pt^{2+}.

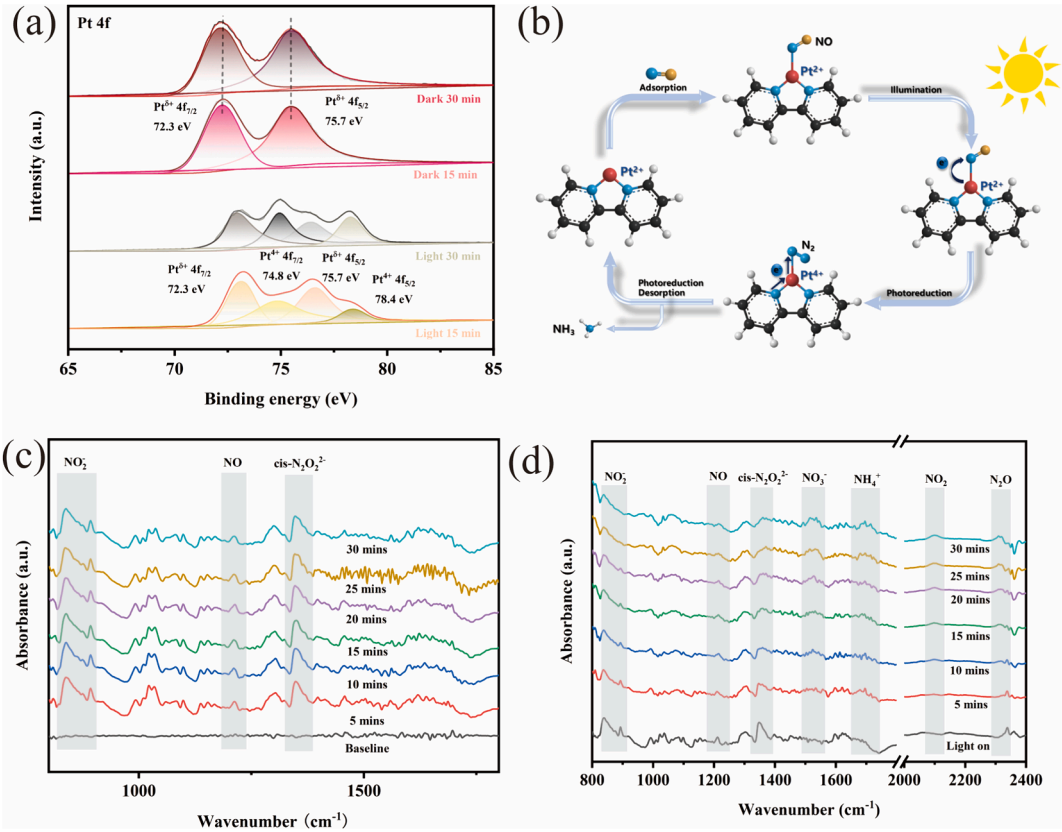

Fig. 10. (a) In-situ XPS result of Pt/40TPBPY-CN during dark and light, (b) Mechanism of Pt^{2+}/Pt^{4+} redox cycle, (c) In-situ DRIFTs of 40Pt-TPBPY-COF during dark and (d) In-situ DRIFTs of 40Pt-TPBPY-COF during light.

under the influence of both light and NO exposure. Remarkably, upon cessation of exposure to both light and NO, the oxidation state of platinum reverts back to + 2, underscoring the reversible nature of this process. The integrated in-situ XPS results and DFT results reveal a proposed reaction pathway on platinum, as depicted in Fig. 10**(b)**. In this proposed pathway, NO molecules initially adsorb onto the Pt^{2+}, facilitating electron transfer from platinum to the nitrogen atom of NO. However, the inherent redox potential proves inadequate to overcome the energy barrier associated with NO reduction. Activation of the light source induces simultaneous photoactivation of platinum and NO, instigating the transfer of photogenerated electron from TP-BPY-COF to platinum. Then, activated Pt^{2+} catalyzes the reduction of NO, wherein the photogenerated electrons transfer from platinum to NO, resulting in the formation of Pt^{4+} and N_2. The third stage of the pathway involves electron-rich Pt^{4+} hindering the desorption of N_2, facilitating the further reduction of N_2 to N-NH. Conforming to the N_2 fixation mechanism, electrons from TP-BPY-CN eventually transition to N-NH for further reduction [36,44]. Throughout this reduction process, N_2 is converted to NH_3 or NH_4^+ and Pt^{4+} undergoes reduction to Pt^{2+} due to electron transfer from TP-BPY-COF, thereby establishing a redox cycle of $Pt^{2+} \rightarrow Pt^{4+} \rightarrow Pt^{2+}$.

3.5.5. *In-situ DRIFTs and NO_3^- and NH_4^+ trapping experiment*

In this study, we also conducted an in-situ Diffuse Reflectance Infrared Fourier Transform Spectroscopy (DRIFTS) experiment. The results, as depicted in Fig. 10**(c)**, reveal distinct bands in the spectral regions of 825–905 cm^{-1}, 970–1060 cm^{-1}, 1100–1250 cm^{-1} and 1300–1400 cm^{-1} under dark conditions. These bands are attributed to NO_2^-, NO, and *cis*-$N_2O_2^{2-}$, respectively [45–48]. Upon irradiation with visible light, new adsorption peaks emerged in Fig. 10**(d)** in the range of 1480–1580 cm^{-1}, 1640–1750 cm^{-1}, 2070 cm^{-1} and 2308 cm^{-1}, corresponding to NO_3^-, NH_4^+, NO_2 and N_2O respectively [49–52]. Significantly, these new peaks became more pronounced with increased irradiation time, while the peaks associated with NO_2^- and NO gradually diminished. These results signify the coexistence of reduction and oxidation products of NO during photocatalytic reactions, and confirm the existence of both reductive and oxidative reaction pathways, which can also be corrobrated by NO_3^- and NH_4^+ trapping experiment (**Text S3**).

3.5.6. *Photocatalytic mechanisms*

In this research, a novel chemically bonded Z-scheme heterostructure was manufactured and the electron transport pathway between these materials progressed from CN to TP-BPY-COF and then to Pt^{2+} are validated by both in-situ XPS and DFT results. The accumulated electrons on the conduction band (CB) of TP-BPY-COF played a pivotal role in the reduction of O_2 to $\bullet O_2^-$ and $\bullet OH$, thereby oxidizing NO to NO_2 and NO_3^-. In addition, the existence of bifunctional single-atom platinum plays a critical role in this photocatalytic system due to its promotion of $\bullet O_2^-$ production and its redox cycle involving Pt^{2+}/Pt^{4+}. In the photocatalytic reaction, NO or O_2 adsorbed on the Pt single atom obtained electron from platinum, facilitating the reduction of NO and O_2 to NH_4^+ and $\bullet O_2^-$, respectively. On the valence band (VB) of CN, the accumulated photogenerated holes were directly oxidized NO to NO_3^-/NO_2, as depicted in Fig. 11. The fabrication of a Z-scheme heterostructure maintained strong oxidative and reductive potential on the VB of CN and CB of TP-BPY-CN, respectively. The introduction of Pt through coordination provided a pathway for the photocatalytic reduction of NO, contributing to an increase in the overall photocatalytic efficiency.

4. Conclusion

In this study, we successfully synthesized an in-situ growth of TP-BPY-COF on the surface of CN and evaluated the impact of different metal ions chelated on TP-BPY-COF concerning photocatalytic

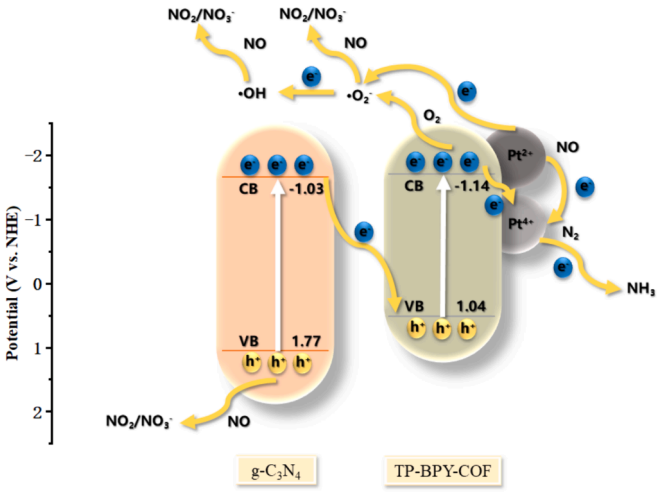

Fig. 11. Photocatalytic oxidation and reduction of NO pathway.

performance. Our research results show that Pt/40TPBPY-CN exhibited improved photocatalytic performance, achieving a 65 % efficiency in the photocatalytic removal of NO under visible light. The interaction between TP-BPY-CN and CN was confirmed through both photoelectrochemical properties and photocatalytic activity tests. The single atom platinum coordinated on TP-BPY-CN not only enhances the photocatalytic oxidation but also facilitates the photocatalytic reduction of NO, further increases the photocatalytic efficiency. Furthermore, the synthesized catalysts exhibit high selectivity for NO_3^- in comparison to CN and demonstrate good stability and recyclability, as evidenced by recycling tests. This work delineates the formation of a Z-scheme heterojunction by leveraging the additional amine groups on CN to enable the in-situ growth of TP-BPY-COF, which possesses extra aldehyde groups, on the surface of CN through Schiff base reactions. Distinct from direct interfacial heterojunctions, this combination strengthens electronic interactions between the two materials through chemical bonding, resulting in strong photocatalytic capabilities. Additionally, the pyridyl groups on TP-BPY-COF provide coordination sites for the loading of single atoms, enhancing their interaction with the heterojunction and offering an additional synthetic pathway for future metal-loaded catalytic materials.

CRediT authorship contribution statement

Zhiyu Xiao: Writing – original draft, Investigation, Formal analysis, Data curation, Conceptualization. **Abubakar Yusuf:** Writing – review & editing, Supervision, Conceptualization. **Yong Ren:** Writing – review & editing, Software, Resources. **George Zheng Chen:** Writing – review & editing, Supervision. **Chengjun Wang:** Writing – review & editing, Resources, Formal analysis. **Jun He:** Writing – review & editing, Supervision, Resources, Project administration, Funding acquisition, Conceptualization.

Declaration of competing interest

The authors declare the following financial interests/personal relationships which may be considered as potential competing interests: Jun He reports financial support was provided by Ningbo Science and Technology Bureau. If there are other authors, they declare that they have no known competing financial interests or personal relationships that could have appeared to influence the work reported in this paper.

Data availability

Data will be made available on request.

Acknowledgements

This work was jointly sponsored by the Ningbo Science and Technology Innovation Key Project (2022Z028), Ningbo Natural Science Foundation Grant (2023J024), Ningbo Commonweal Key Research Program (2023S038) and Ningbo Key Technology Breakthrough Scheme Projects under Yongjiang Science and Innovation 2035 projects (2024Z237, 2024Z251).

Appendix A. Supplementary data

Supplementary data to this article can be found online at https://doi.org/10.1016/j.cej.2024.154487.

References

[1] F. Li, G. Liu, F. Liu, J. Wu, S. Yang, Synergetic effect of CQD and oxygen vacancy to TiO_2 photocatalyst for boosting visible photocatalytic NO removal, J. Hazard. Mater. 452 (2023) 131237.
[2] Y. Xin, Q. Zhu, T. Gao, X. Li, W. Zhang, H. Wang, D. Ji, Y. Huang, M. Padervand, F. Yu, C. Wang, Photocatalytic NO removal over defective Bi/BiOBr nanoflowers: The inhibition of toxic NO_2 intermediate via high humidity, Appl Catal B 324 (2023) 122238.
[3] K. Li, W. Zhou, X. Li, Q. Li, S.A.C. Carabineiro, S. Zhang, J. Fan, K. Lv, Synergistic effect of cyano defects and $CaCO_3$ in graphitic carbon nitride nanosheets for efficient visible-light-driven photocatalytic NO removal, J. Hazard. Mater. 442 (2023) 130040.
[4] H. Ma, W. Yang, H. Tang, Y. Pan, W. Li, R. Fang, Y. Shen, F. Dong, Enhance the stability of oxygen vacancies in $SrTiO_3$ via metallic Ag modification for efficient and durable photocatalytic NO abatement, J. Hazard. Mater. 452 (2023) 131269.
[5] L. Han, J. Huang, J. Zhan, X. Zhang, S. Wang, H. Chen, Construction of Highly Dispersed Ni Sites on N-rich Carbon Nitride for Enhanced Photocatalytic NO Removal, Advanced Sustainable Systems 7 (2023) 2200009.
[6] N. Li, C. Wang, K. Zhang, H. Lv, M. Yuan, D.W. Bahnemann, Progress and prospects of photocatalytic conversion of low-concentration NO_x, Chin. J. Catal. 43 (2022) 2363–2387.
[7] C. Nie, X. Wang, P. Lu, Y. Zhu, X. Li, H. Tang, Advancements in S-scheme heterojunction materials for photocatalytic environmental remediation, J. Mater. Sci. Technol. 169 (2024) 182–198.
[8] Z. Ajmal, M.u. Haq, Y. Naciri, R. Djellabi, N. Hassan, S. Zaman, A. Murtaza, A. Kumar, A.G. Al-Sehemi, H. Algarni, O.A. Al-Hartomy, R. Dong, A. Hayat, A. Qadeer,, Recent advancement in conjugated polymers based photocatalytic technology for air pollutants abatement: Cases of CO_2, NO_x, and VOCs, Chemosphere 308 (2022) 136358.
[9] Y. Tang, W. Cui, S. Wang, F. Dong, Efficient photocatalytic NO removal with inhibited NO_2 formation and catalyst loss over sponge-supported and functionalized g-C_3N_4, J. Hazard. Mater. 465 (2024) 133323.
[10] B. Liu, H. Huang, Z. Xiao, J. Yang, M. Zhu, 2D/3D g-C_3N_4/BiOI heterostructure catalyst for efficient and robust photocatalytic NO removal, Sep. Purif. Technol. 310 (2023) 123183.
[11] X. Wu, N. Kang, X. Li, Z. Xu, S.A.C. Carabineiro, K. Lv, 2D/2D layered BiOIO3/g-C3N4 S-scheme heterojunction for photocatalytic NO oxidation, J. Mater. Sci. Technol. 196 (2024) 40–49.
[12] B. Zhang, X. Hu, E. Liu, J. Fan, Novel S-scheme 2D/2D BiOBr/g-C_3N_4 heterojunctions with enhanced photocatalytic activity, Chin. J. Catal. 42 (2021) 1519–1529.
[13] Z. Chen, J. Wang, M. Hao, Y. Xie, X. Liu, H. Yang, G.I.N. Waterhouse, X. Wang, S. Ma, Tuning excited state electronic structure and charge transport in covalent organic frameworks for enhanced photocatalytic performance, Nat. Commun. 14 (2023) 1106.
[14] T. He, W. Zhen, Y. Chen, Y. Guo, Z. Li, N. Huang, Z. Li, R. Liu, Y. Liu, X. Lian, C. Xue, T.C. Sum, W. Chen, D. Jiang, Integrated interfacial design of covalent organic framework photocatalysts to promote hydrogen evolution from water, Nat. Commun. 14 (2023) 329.
[15] Y. Yang, X. Chu, H.-Y. Zhang, R. Zhang, Y.-H. Liu, F.-M. Zhang, M. Lu, Z.-D. Yang, Y.-Q. Lan, Engineering β-ketoamine covalent organic frameworks for photocatalytic overall water splitting, Nat. Commun. 14 (2023) 593.
[16] Z. Xia, Y. Zhao, S.B. Darling, Covalent Organic Frameworks for Water Treatment, Adv. Mater. Interfaces 8 (2021) 2001507.
[17] Z. Yang, J. Liu, Y. Li, G. Zhang, G. Xing, L. Chen, Arylamine-Linked 2D Covalent Organic Frameworks for Efficient Pseudocapacitive Energy Storage, Angew. Chem. Int. Ed. 60 (2021) 20754–20759.
[18] E.A. Gendy, J. Ifthikar, J. Ali, D.T. Oyekunle, Z. Elkhlifia, I.I. Shahib, A.I. Khodair, Z. Chen, Removal of heavy metals by covalent organic frameworks (COFs): A review on its mechanism and adsorption properties, J. Environ. Chem. Eng. 9 (2021) 105687.
[19] E.A. Gendy, D.T. Oyekunle, J. Ifthikar, A. Jawad, Z. Chen, A review on the adsorption mechanism of different organic contaminants by covalent organic framework (COF) from the aquatic environment, Environ. Sci. Pollut. Res. 29 (2022) 32566–32593.

[20] J. Ifthikar, D.T. Oyekunle, A. Jawad, B. Wu, J. Hongwu, H. Yezi, Y. Lie, E.A. Gendy, J. Wang, I.I. Shahib, Z. Chen, Study on the coordination conduct and kinetic insights within the oxo-vanadate and organic reductive nitrogen and sulfur functionalities during the reduction coupled adsorption processes: Implications in practical applications, J. Hazard. Mater. 448 (2023) 130810.
[21] J. Lv, Y.-X. Tan, J. Xie, R. Yang, M. Yu, S. Sun, M.-D. Li, D. Yuan, Y. Wang, Direct Solar-to-Electrochemical Energy Storage in a Functionalized Covalent Organic Framework, Angew. Chem. Int. Ed. 57 (2018) 12716–12720.
[22] Z. Xiao, Y. Ren, G.Z. Chen, Y. Sun, C. Wang, J. He, Study of pyrene-based covalent organic frameworks for efficient photocatalytic oxidation of low-concentration NO, J. Environ. Chem. Eng. 12 (2024) 113470.
[23] Y. Zhang, Z. Hu, H. Zhang, H. Li, S. Yang, Uncovering Original Z Scheme Heterojunctions of COF/MO_x (M = Ti, Zn, Zr, Sn, Ce, and Nb) with Ascendant Photocatalytic Selectivity for Virtually 99.9% NO-to-NO^{3-} Oxidation, Adv. Funct. Mater. 33 (2023) 2303851.
[24] J. Chen, X. Tao, C. Li, Y. Ma, L. Tao, D. Zheng, J. Zhu, H. Li, R. Li, Q. Yang, Synthesis of bipyridine-based covalent organic frameworks for visible-light-driven photocatalytic water oxidation, Appl Catal B 262 (2020) 118271.
[25] R. Sun, X. Hu, C. Shu, L. Zheng, S. Wang, X. Wang, B. Tan, Anchoring single Co sites on bipyridine-based covalent triazine framework for efficient photocatalytic oxygen evolution, Chin. J. Catal. 55 (2023) 159–170.
[26] X. Li, S. Yang, M. Liu, S. Liu, Q. Miao, Z. Duan, P. Qiao, J. Lin, F. Sun, Q. Xu, Z. Jiang, Immobilization of Platinum Nanoparticles on Covalent Organic Framework-Derived Carbon for Oxygen Reduction Catalysis, Small Structures 4 (2023) 2200320.
[27] S. Qin, N. Denisov, H. Kim, P. Schmuki, Photocatalytic H_2 Generation: Controlled and Optimized Dispersion of Single Atom Co-Catalysts Based on Pt-TCPP Planar Adsorption on TiO_2, Angew. Chem. Int. Ed. 63 (2024) e202316660.
[28] Z. Xiao, H. Do, A. Yusuf, H. Jia, H. Ma, S. Jiang, J. Li, Y. Sun, C. Wang, Y. Ren, G. Z. Chen, J. He, Facile synthesis of multi-layer $Co(OH)_2/CeO_2$-g-C_3N_4 ternary synergistic heterostructure for efficient photocatalytic oxidation of NO under visible light, J. Hazard. Mater. 462 (2024) 132744.
[29] L.-L. Liu, F. Chen, J.-H. Wu, J.-J. Chen, H.-Q. Yu, Synergy of crystallinity modulation and intercalation engineering in carbon nitride for boosted H_2O_2 photosynthesis, Proc. Natl. Acad. Sci. 120 (2023) e2215305120.
[30] M. Liu, S. Liu, Q. Xu, Q. Miao, S. Yang, S. Hanson, G.Z. Chen, J. He, Z. Jiang, G. Zeng, Dual atomic catalysts from COF-derived carbon for CO_2RR by suppressing HER through synergistic effects, Carbon Energy 5 (2023) e300.
[31] Q. Miao, S. Yang, Q. Xu, M. Liu, P. Wu, G. Liu, C. Yu, Z. Jiang, Y. Sun, G. Zeng, Constructing Synergistic Zn-N_4 and Fe-N_4O Dual-Sites from the COF@MOF Derived Hollow Carbon for Oxygen Reduction Reaction, Small Structures 3 (2022) 2100225.
[32] D. Liu, D. Chen, N. Li, Q. Xu, H. Li, J. He, J. Lu, Surface Engineering of g-C_3N_4 by Stacked BiOBr Sheets Rich in Oxygen Vacancies for Boosting Photocatalytic Performance, Angew. Chem. Int. Ed. 59 (2020) 4519–4524.
[33] X. Liu, Z. Hao, H. Wang, T. Wang, Z. Shen, H. Zhang, S. Zhan, J. Gong, Enhanced localized dipole of Pt-Au single-site catalyst for solar water splitting, Proceedings of the National Academy of Sciences, 119 (2022) e2119723119.
[34] Y. Zheng, Y. Jiao, Y. Zhu, Q. Cai, A. Vasileff, L.H. Li, Y. Han, Y. Chen, S.-Z. Qiao, Molecule-Level g-C_3N_4 Coordinated Transition Metals as a New Class of Electrocatalysts for Oxygen Electrode Reactions, J. Am. Chem. Soc. 139 (2017) 3336–3339.
[35] S. Dutta, S.K. Pati, Anchoring boron on a covalent organic framework as an efficient single atom metal-free photo-electrocatalyst for nitrogen fixation: a first-principles analysis, PCCP 24 (2022) 10765–10774.
[36] G. Ren, M. Shi, Z. Li, Z. Zhang, X. Meng, Electronic metal-support interaction via defective-induced platinum modified BiOBr for photocatalytic N_2 fixation, Appl Catal B 327 (2023) 122462.
[37] S. Hejazi, S. Mohajernia, B. Osuagwu, G. Zoppellaro, P. Andryskova, O. Tomanec, S. Kment, R. Zbořil, P. Schmuki, On the Controlled Loading of Single Platinum Atoms as a Co-Catalyst on TiO_2 Anatase for Optimized Photocatalytic H_2 Generation, Adv. Mater. 32 (2020) 1908505.
[38] L. Gong, Q. Chu, X. Liu, Y. Tan, Plasmonic platinum nanoparticles–tungsten oxide nanoarchitectures as visible light photocatalysts for highly efficient overall water splitting, J. Mater. Chem. A 10 (2022) 21161–21176.
[39] I.I. Sadykov V.L. Sushkevich F. Krumeich R.J.G. Nuguid J.A. van Bokhoven M. Nachtegaal O.V. Safonova Platinum-Iron(II) Oxide Sites Directly Responsible for Preferential Carbon Monoxide Oxidation at Ambient Temperature: An Operando X-ray Absorption Spectroscopy Study** Angew. Chem. Int. Ed. 62 2023 e202214032.
[40] J. Liu, J. Liao, K. Huang, J. Dong, G. He, Z. Gong, H. Fei, A General Strategy to Remove Metal Aggregates toward Metal–Nitrogen–Carbon Catalysts with Exclusive Atomic Dispersion, Adv. Mater. 35 (2023) 2211398.
[41] W. Chen, X. Zhu, W. Wei, H. Chen, T. Dong, R. Wang, M. Liu, K. Ostrikov, P. Peng, S.-Q. Zang, Neighboring Platinum Atomic Sites Activate Platinum-Cobalt Nanoclusters as High-Performance ORR/OER/HER Electrocatalysts, Small 19 (2023) 2304294.
[42] P. Zhou, I.A. Navid, Y. Ma, Y. Xiao, P. Wang, Z. Ye, B. Zhou, K. Sun, Z. Mi, Solar-to-hydrogen efficiency of more than 9% in photocatalytic water splitting, Nature 613 (2023) 66–70.
[43] Z. Li, R. Li, H. Jing, J. Xiao, H. Xie, F. Hong, N. Ta, X. Zhang, J. Zhu, C. Li, Blocking the reverse reactions of overall water splitting on a Rh/GaN–ZnO photocatalyst modified with Al_2O_3, Nat. Catal. 6 (2023) 80–88.
[44] J. Zhang, L. Yue, Z. Zeng, C. Zhao, L. Fang, X. Hu, H. Lin, L. Zhao, Y. He, Preparation of $NaNbO_3$ microcube with abundant oxygen vacancies and its high photocatalytic N_2 fixation activity in the help of Pt nanoparticles, J. Colloid Interface Sci. 636 (2023) 480–491.
[45] Y. Ren, Y. Li, X. Wu, J. Wang, G. Zhang, S-scheme Sb_2WO_6/g-C_3N_4 photocatalysts with enhanced visible-light-induced photocatalytic NO oxidation performance, Chin. J. Catal. 42 (2021) 69–77.
[46] Y. Zhou, Z. Zhao, F. Wang, K. Cao, D.E. Doronkin, F. Dong, J.-D. Grunwaldt, Facile synthesis of surface N-doped $Bi_2O_2CO_3$: Origin of visible light photocatalytic activity and in situ DRIFTS studies, J. Hazard. Mater. 307 (2016) 163–172.
[47] H. Ma, Y. He, X. Li, J. Sheng, J. Li, F. Dong, Y. Sun, In situ loading of MoO_3 clusters on ultrathin Bi_2MoO_6 nanosheets for synergistically enhanced photocatalytic NO abatement, Appl Catal B 292 (2021) 120159.
[48] E. Gao, H. Pan, W. Zhang, Y. Li, G. Cao, M.T. Bernards, Y. He, Y. Shi, Insights on the mechanism of enhanced selective catalytic reduction of NO with NH_3 over Zr-doped $MnCr_2O_4$: A combination of in situ DRIFTS and DFT, Chem. Eng. J. 386 (2020) 123956.
[49] W. Zhang, Y. Wang, Y. Wang, Y. Liang, F. Dong, Highly efficient photocatalytic NO removal and in situ DRIFTS investigation on $SrSn(OH)_6$, Chin. Chem. Lett. 33 (2022) 1259–1262.
[50] Y. Shi, X. Wang, L. Chen, S. Li, C. Wu, S. Shan, W. Li, In situ DRIFT study on NH_3 selective catalytic reduction of NO_x over HBEA zeolite doped with CeO_2, Appl. Surf. Sci. 506 (2020) 144715.
[51] J. Li, P. Yan, K. Li, W. Cen, X. Yu, S. Yuan, Y. Chu, Z. Wang, Generation and transformation of ROS on g-C_3N_4 for efficient photocatalytic NO removal: A combined in situ DRIFTS and DFT investigation, Chin. J. Catal. 39 (2018) 1695–1703.
[52] H. Zhu, Y. Li, X. Zheng, In-situ DRIFTS study of CeO_2 supported Rh catalysts for N_2O decomposition, Appl. Catal. A 571 (2019) 89–95.